Molecular fingerprints of star formation throughout the Universe : a space-based infrared study

Lahuis, F.

Chapter 4

ISO-SWS Spectroscopy of Gas-Phase C_2H_2 and HCN Toward Massive Young Stellar Objects

Abstract

Observations of gas-phase C_2H_2 and HCN along the line of sight toward a large sample of deeply embedded massive young stellar objects (YSOs) have been performed using the Short Wavelength Spectrometer on board the Infrared Space Observatory. The ν_5 vibration-rotation band of C_2H_2 around $13.7\,\mu$m and the ν_2 band of HCN around $14.0\,\mu$m have been detected for most lines of sight. These wavelength regions are heavily affected by instrumental fringing and a detailed discussion of the data reduction techniques is given. Comparison with model spectra allows the excitation temperatures and the abundances of the molecules to be determined. The inferred excitation temperatures range from < 100 to 1000 K, and correlate well with each other, indicating that the two molecules probe the same warm gas component. The C_2H_2 and HCN column densities increase by more than an order of magnitude with increasing excitation temperature, and with the amount of heating of the ices. The corresponding abundances of C_2H_2 and HCN in the warm gas increase from $\sim 10^{-8}$ to $\sim 10^{-6}$ with increasing temperatures. The enhanced abundances are compared with a variety of chemical models. The observed gas-phase C_2H_2 most likely results from direct evaporation of interstellar ices, where C_2H_2 must be present at an abundance of $\sim 0.1 - 0.5\,\%$ with respect to H_2O ice. This abundance is consistent with the measured amount of C_2H_2 in cometary ices. The observed gas-phase HCN abundance shows a stronger increase with temperature and results from a combination of evaporation of ices and high-temperature gas-phase chemistry in the hot core.

Lahuis, F., & van Dishoeck, E.F. 2000, $A\&A$, 355, 699

4.1 Introduction

Infrared absorption spectroscopy of gas-phase molecules can provide important complementary information on the physical and chemical structure of sources compared with submillimeter emission line data (Mitchell et al., 1990; Evans et al., 1991; Carr et al., 1995). Molecules without dipole moments such as C_2H_2 and CH_4, which are among the most abundant carbon-bearing molecules, can only be observed through their vibration-rotation infrared spectra (Lacy et al., 1989, 1991). An additional advantage of infrared spectroscopy is that the full rotational population distribution of the molecule in its lowest vibrational state is obtained in a single infrared spectrum, whereas multiple frequency settings are needed at submillimeter wavelengths, often involving different telescopes and/or receivers. This allows direct constraints on the excitation conditions, in particular the temperature and density structure of the region. The infrared absorption data refer to pencil-beam lines of sight toward bright infrared sources, most of which are deeply embedded massive young stellar objects (YSOs). Such observations are therefore powerful probes of the chemical evolution of the gas and dust during the earliest stages of star formation (see van Dishoeck & Blake, 1998; Langer et al., 2000; van Dishoeck & Hogerheijde, 1999, for recent reviews) In this paper, observations of two molecules, C_2H_2 and HCN, obtained with the Short Wavelength Spectrometer (SWS) on board the Infrared Space Observatory (ISO) are used to probe the chemistry and temperature structure of the warm gas close to the massive YSOs.

The ISO-SWS provides the first opportunity for vibration-rotation spectroscopy of gas-phase molecules above the Earth's atmosphere. Although the low resolving power $R = \lambda/\Delta\lambda \approx 2000$ of the grating spectrometer prevents the detection of minor gas-phase species, abundant molecules such as H_2O, CO_2 and CH_4 have been seen with the SWS (e.g. Helmich, 1996; van Dishoeck & Helmich, 1996; Boogert et al., 1998; van Dishoeck, 1998; Dartois et al., 1998; Boonman et al., 1999), The observations of C_2H_2 and HCN presented here provide significant complementary information. C_2H_2 forms an important building block in the gas-phase formation of large organic molecules. For example, reactions of C_2H_2 with C^+, C and small radicals lead to long unsaturated carbon chains, whereas reactions with CN produce cyanopolyynes such as HC_3N (Herbst, 1995). HCN is one of the more abundant nitrogen-bearing molecules in dense clouds, and has, in contrast with C_2H_2, a large dipole moment. Since HCN can also be observed at submillimeter wavelengths, the combination of the infrared and submillimeter data provides important constraints on the source structure (Carr et al., 1995; van der Tak et al., 1999, 2000).

A major strength of infrared spectroscopy is that not only gas-phase molecules, but also the complementary solid-state species can be detected for the same line of sight. The gas/solid ratios of H_2O, CO_2 and CH_4 provide a new probe of the temperature structure and the evolutionary state of the objects (van Dishoeck et al., 1996; Boogert et al., 1998; Dartois et al., 1998; van Dishoeck, 1998) Moreover, the structure of the ice bands, in particular that of solid CO_2, gives a direct indication of the thermal history of the ices (Ehrenfreund et al., 1997; Gerakines et al., 1999; Boogert et al., 2000) Solid C_2H_2 and HCN have not yet been detected, but limits are available from ground-based and ISO data (Boudin et al., 1998, Schutte 1998, private communication).

Table 4.1. Summary of observed sources

Target	R.A. (2000)	Dec (2000)	Obs. ID	Flux[a] (Jy)[a]	$L/L_\odot$ (10^5)	d (kpc)	Ref.[b]
AFGL 2136	$18^h\,22^m\,26^s.3$	$-13°\,30'\,08''$	12000925	280	0.7	2	1
AFGL 2591	$20^h\,29^m\,24^s.7$	$+40°\,11'\,19''$	19301928	910	0.2	1	1
AFGL 4176	$13^h\,43^m\,02^s.1$	$-62°\,08'\,52''$	11701404	430	1.8	4	2, 3
AFGL 4176	$13^h\,43^m\,02^s.1$	$-62°\,08'\,52''$	30601344	360	1.8	4	2, 3
NGC 3576	$11^h\,11^m\,53^s.9$	$-61°\,18'\,25''$	29200143	280	3.5	2.4	4, 3
NGC 7538 IRS 1	$23^h\,13^m\,45^s.4$	$+61°\,28'\,09''$	28301235	360	1.3	2.8	1
NGC 7538 IRS 9	$23^h\,14^m\,01^s.6$	$+61°\,27'\,21''$	28301334	80	0.4	2.8	1
W 33 A	$18^h\,14^m\,39^s.4$	$-17°\,52'\,01''$	46700521	50	1.0	4	1
W 3 IRS 5	$02^h\,25^m\,40^s.9$	$+62°\,05'\,52''$	42701224	750	1.7	2.2	1
S 140 IRS 1	$22^h\,19^m\,18^s.2$	$+63°\,18'\,47''$	26301731	520	0.2	0.9	1
G 333.3–0.4	$16^h\,21^m\,30^s.9$	$-50°\,25'\,07''$	45800340	150	6	3.9	5, 3
AFGL 2059	$18^h\,04^m\,53^s.0$	$-24°\,26'\,45''$	49302585	160	0.16	1.5	2, 3

[a] Average flux from 13.5 to 14 μm derived from ISO–SWS spectra.

[b] Sources of luminosities and distances; (1) van der Tak et al. (1999, 2000), (2) Distance from Henning et al. (1990) (3) Luminosity derived from ISO spectra, (4) Distance from Persi et al. (1987), and (5) Distance from Azcarate et al. (1986)

Some infrared lines in the ν_5 C_2H_2 bending mode at $13.7\,\mu$m and ν_2 HCN bending mode at $14.0\,\mu$m have been previously observed from the ground at high spectral resolution $R = \lambda/\Delta\lambda \approx 10,000$ by Lacy et al. (1989); Evans et al. (1991); Carr et al. (1995) in a few sources. These bands have been selected owing to their large oscillator strengths and because the infrared sources are up to an order of magnitude brighter at $14\,\mu$m than at $3 - 4\,\mu$m, where the corresponding stretching vibrations occur. The lower-resolution ISO data presented here cannot resolve the individual vibration-rotation lines, but can be used to detect the strong Q-branch without atmospheric interference in a much larger number of objects. Comparison with model profiles allows the physical conditions to be constrained over a wider range of parameters (Helmich, 1996). Unfortunately, the efficiency of the higher-resolution Fabry-Pérot of the ISO-SWS was too low to survey a large number of sources in HCN and C_2H_2 in a reasonable integration time.

In the following, we discuss first the observational data for C_2H_2 and HCN, with special emphasis on the data reduction techniques that have been used to extract the very weak lines (§4.2). We subsequently compare the observations with theoretical profiles constructed using a simple excitation model (§4.3). The resulting excitation temperatures are compared with each other and with those found for other molecules (§4.4). Finally, the inferred abundances are discussed in the context of the physical and chemical evolution of the sources (§4.5). An initial account has been given by Lahuis & van Dishoeck (1997).

4.2 Observations and data reduction

4.2.1 Observations and sources

Table 4.1 summarises the sources and the observational data used in this study. All objects are deeply embedded massive young stars with luminosities ranging from $10^4 - 2 \times 10^5\ L_\odot$ for which complementary ISO data on ices and other gas-phase molecules are available. In addition, high-resolution gas-phase CO and ^{13}CO data have been obtained for most of the sources by Mitchell et al. (1990), from which information on the total column densities and excitation temperatures of both the hot and the cold gas along the lines of sight can be derived. Orion IRc2/BN is not included in this study, but is discussed separately by Boonman et al. (1999).

All observations were performed with the ISO-SWS mode AOT06 at full grating resolution (de Graauw et al., 1996). The wavelength range scanned was typically $12 - 16\,\mu$m (AOT-band 3A). The spectral region used in the analysis of the C_2H_2 and HCN bands is only $13.4 - 14.4\,\mu$m, but the larger observed spectral range is necessary for a proper removal of instrumental fringes. The resolving power at these wavelengths is $R \approx 1800$, corresponding to $\sim 165\,\mathrm{km\,s^{-1}}$. Thus, the lines are not resolved.

4.2.2 Data reduction

Our reduction is performed within the SWS Interactive Analysis system IA^3 developed and used within the ISO-SWS consortium. For a detailed description of IA^3 see Roelfsema et al. (1993); Wieprecht et al. (1998); Lahuis et al. (1998). The adopted reduction method uses a combination of standard pipeline software (version 7) and additional IA^3 software. The pipeline software is identical to the software used in the ISO Standard Product Generation software which generates the data products distributed to the ISO observers and contained in the ISO data archive.

The depth of the C_2H_2 and HCN features is less than $10\,\%$ of the continuum (for some observations of the order of $1 - 2\,\%$) at the resolution of the ISO-SWS grating. The ISO-SWS grating spectra in this spectral region are heavily affected by instrumental fringing which makes the identification and analysis of weak features very difficult. Special data reduction techniques need to be applied in order to extract these weak features.

4.2.2.1 Fringe removal

The main problem is the application of the Relative Spectral Response Function (RSRF), which is dominated by instrumental fringing in this wavelength region. This fringing is the result of the Fabry-Pérot effect within the ISO-SWS instrument at a number of locations in the light-path. Some of the properties of these interferences, in particular their shape and amplitude, change depending on the orientation and location of the source in the ISO-SWS aperture and are therefore different from source to source. The RSRF was derived in the laboratory using a fully extended blackbody source, whereas our astronomical sources are not fully extended and thus have a different fringe pattern. The net result of these effects is that it is difficult to correct for the fringes in the standard pipeline processing.

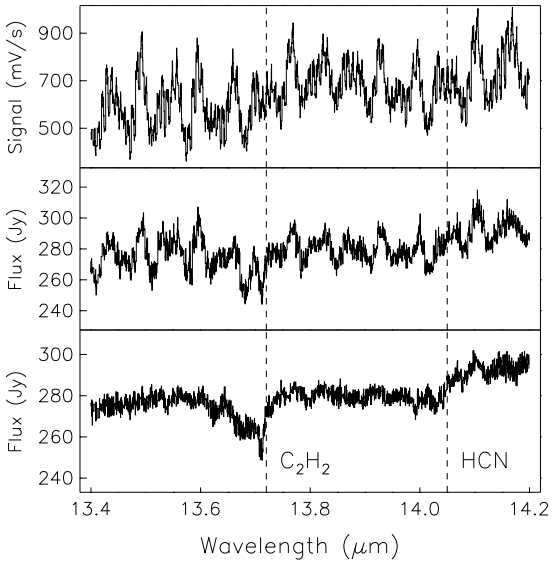

Figure 4.1 Example of the impact of fringes in the $13.4 - 14.4\,\mu$m (band 3A) part of the spectrum for AFGL 2136. In the top plot, the raw signal from the twelve detectors covering this spectral range is shown, in which the instrumental fringing is evident. The middle plot shows the result for all twelve detectors as produced with standard processing: large fringe residuals remain making the detection of weak spectral features very difficult. In the bottom plot, the result of improved data reduction is shown. Note the different flux scale. The fringe residuals are low and allow detection of spectral features of only a few percent. The vertical lines indicate the positions of the ν_5 vibration-rotation band of C_2H_2 and the ν_2 vibration-rotation band of HCN.

The amplitude of the remaining fringe-residuals after the application of the RSRF can be reduced significantly, however, by applying (any or a combination of) the following reduction methods within IA^3:

- correcting for shifts caused by pointing or wavelength calibration inaccuracies via a cross-correlation of the data and the RSRF
- enhancing the amplitude of the RSRF to match the amplitude of the fringes in the data
- removing the fringe-residuals by fitting sinusoids or by Fourier filtering

For our reduction, we first made a shift and amplitude correction to the RSRF before applying it. Subsequently, we removed the residual fringes by fitting sinusoids. The two dedicated IA^3 routines `RESP_INTER` and `FRINGES` have been used for this purpose.

In principle this procedure allows removal of the fringe residuals to a level of less than $1\,\%$, resulting in spectra with a signal-to-noise ratio on the continuum of 100 or better. However the presence of spectral features may complicate the application of these tools, especially if they have some regularity such as the P- and R-branches of molecular spectra. To test the stability of this procedure on the C_2H_2 and HCN molecular data, tests were made using synthetic spectra at a few different temperatures (and thus with more or less prominent P- and R-branches). The relative effect of the fringe

removal on the synthetic spectra is small, of the order of $1-2\,\%$ (i.e. $\leq 0.1\,\%$ in the continuum subtracted spectra assuming a depth of the features of $10\,\%$ or less), provided a large enough wavelength range is used.

With the current status of the calibration and data analysis, the unresolved Q-branches of C_2H_2 and HCN are clearly detected in most sources. However, it is not possible to analyse the corresponding P- and R-branch lines separately, since they have an absorption depth of approximately $0.5-1\,\%$ or less. In most cases this is close to the noise level and the amplitude of the fringe-residuals after the fringe removal. Individual lines may match with observed features and are probably real, but they cannot be used as a decisive argument in favour of a particular model. They can, however, help to constrain the fits in some cases, e.g. to exclude a temperature or column density on the basis of the lack of detected P- and R-branch lines.

4.3 Model spectra and fits

Figure 4.2 illustrates the synthetic spectra of the HCN $\nu_2 = 1-0$ band at $R \approx 30,000$ and 1800 for an excitation temperature of 300 K, a typical column density of $1.\,10^{16}\,\mathrm{cm}^{-2}$ and $b = 5\,\mathrm{km\,s}^{-1}$. The Q-branch in the lower resolution spectrum is clearly unresolved and less deep than in the higher resolution spectrum and the P- and R-branch lines become weak, making their detection difficult. However, the Q-branch consisting of many blended lines results in strong enough absorption to be detected, even at the

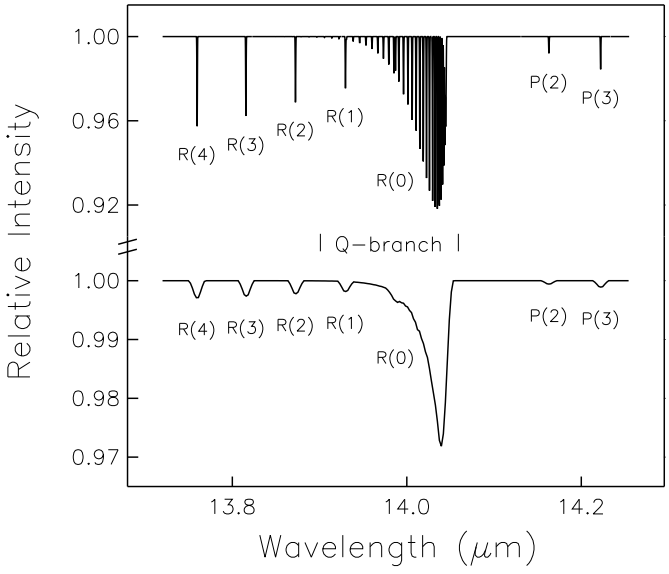

Figure 4.2 The Q-branch and lowest P- and R-branch lines of HCN at a resolving power of 30,000 and 1800 (reflecting the approximate resolutions of the ISO-SWS FP and grating in this spectral region), an excitation temperature of 300 K and a column density of $1.\,10^{16}\,\mathrm{cm}^{-2}$ and $b = 5\,\mathrm{km\,s}^{-1}$. The P- and R-branch lines are marked in the spectra.

Table 4.2. HCN fundamental and ν_2 low-lying vibrational transitions

transition	$\nu_i\,(\mathrm{cm}^{-1})$	d_i	state	$\nu_i\,(\mathrm{cm}^{-1})^a$	d_i
fundamental transitions			ν_2 vibrational states		
$\nu_1\,(10^00)^b$	3311.5	1	(01^10)	711.98	2
$\nu_2\,(01^10)^a$	711.98	2	(02^00)	1411.41	1
$\nu_3\,(00^01)^c$	2096.8	1	(02^20)	1426.53	2
			(03^10)	2113.45	2
			(03^30)	2143.76	2
$\nu_2\,\mathrm{H}^{13}\mathrm{CN}^a$	705.97				
$\nu_2\,\mathrm{HC}^{15}\mathrm{N}^a$	711.03				

Molecular data from; (*a*) Duxbury & Gang (1989) (*b*) Choe et al. (1986), and (*c*) Choe et al. (1987)

lower resolution. The asymmetric shape of the Q-branch and the relative strength of the Q-branches originating from vibrationally excited levels can be used to constrain the excitation temperature (see §4.3.2). The depth is then used to determine the column density. It is these features which make vibrational bands of molecules with a Q-branch particularly well suited for low-resolution observations. The same holds for the Q-branch of the C_2H_2 ν_5 band presented in this paper. Another excellent example is provided by the ν_2 bending mode of CO_2, which has its Q-branch at $14.98\,\mu$m (e.g. van Dishoeck et al., 1996; Boonman et al., 1999).

4.3.1 Synthetic spectra

Model C_2H_2 and HCN spectra have been constructed assuming that the population distribution is in local thermodynamic equilibrium (LTE). For a rotational level J in the ground vibrational state,

$$\frac{N_J}{N} = \frac{g_n(2J+1)e^{-E_J/kT}}{Q(T)} \tag{4.1}$$

with N the total column density, E_J the energy of level J, and g_n the nuclear statistical weight with $g_n = 1$ for even J and $g_n = 3$ for odd J in the case of C_2H_2, and $g_n = 1$ for all J in the case of HCN. The partition function, $Q(T)$, is the product of the rotational partition function, $Q_r(T)$,

$$Q_r = \sum_J g_n(2J+1)e^{-E_J/kT} \tag{4.2}$$

summed over all levels J, and the vibrational partition function, $Q_v(T)$, which can be approximated by the product

$$Q_v \approx \prod_i (1 - e^{-E_{v_i}/kT})^{-d_i} \tag{4.3}$$

over all fundamental vibrational transitions v_i. Table 4.2 lists the frequencies ν_i and degeneracies d_i of all fundamental transitions of HCN and of the lower vibrationally

exited levels of the HCN ν_2 mode. At low temperatures, $T \ll 300\,\mathrm{K}$, Q_v goes to unity and thus the fraction of molecules in the vibrationally excited levels is negligible.

The fractional population in a vibrationally exited level is:

$$x_{v_i} = \frac{d_i e^{-E_{v_i}/kT}}{Q_v}. \tag{4.4}$$

Line oscillator strengths are derived from the transition probabilities listed in the HITRAN database (edition 1992, Rothman et al., 1992).

$$f_{ul} = 4.701755 \times 10^{-7} \nu R_{ul} \tag{4.5}$$

with the transition probability R_{ul} in Debye^2.

Using the populations in each level, the optical depths are calculated assuming a Voigt profile function. The final spectrum is reduced to the resolution of the observed ISO-SWS grating spectrum using a Gaussian profile.

Figure 4.3 illustrates the column densities at which the strongest C_2H_2 and HCN lines in the bands become optically thick for Doppler parameters b of $1.5,\ 5$ and $10\,\mathrm{km\,s^{-1}}$. Typical column densities for our sources range from a few$\times 10^{15}$ to a few$\times 10^{16}$ cm^{-2} (see §4). Thus, optical depth effects become significant only for C_2H_2 in cold sources with $b < 5$ km s^{-1} and $N(C_2H_2) > 10^{15}$ cm^{-2}. Our sample contains only one such object (W 33A, see §4.4), and for this source an accurate knowledge of the b value is needed to derive reliable column densities. In all other cases, the excitation temperatures are high and the results are not sensitive to the adopted value of b.

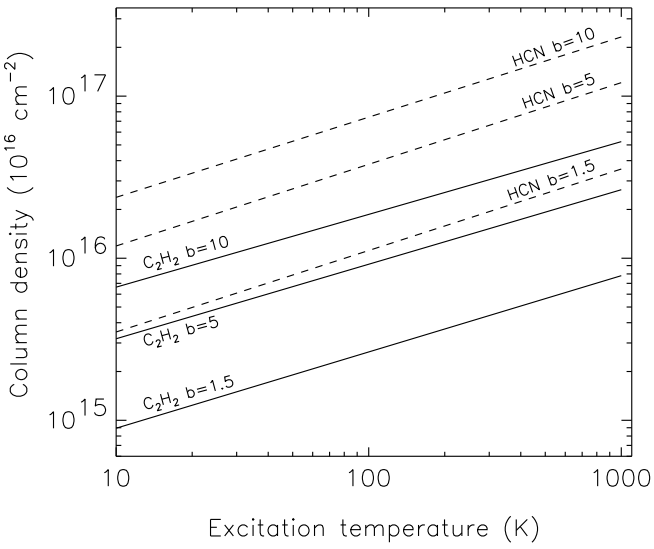

Figure 4.3 Column densities at which the strongest C_2H_2 and HCN absorption lines become optically thick ($\tau = 1$) for Doppler parameters b of $1.5,\ 5$ and $10\,\mathrm{km\,s^{-1}}$ at excitation temperatures from 10 to 1000 K.

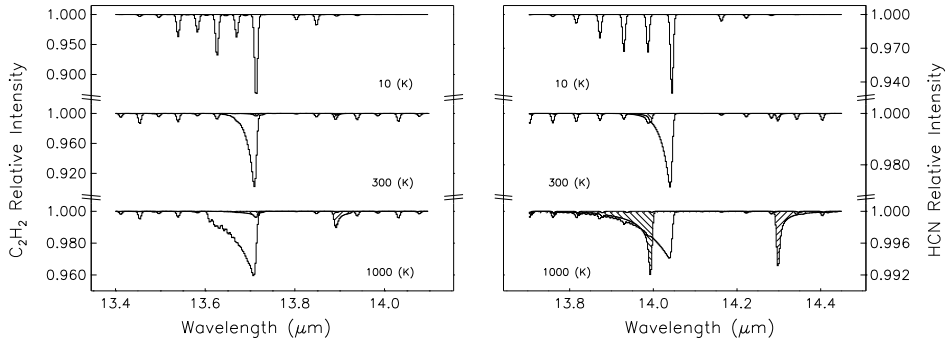

(a) C_2H_2 $\nu_5 = 1-0$ fundamental and $\nu_5 = 2-1$ hot bands.

(b) HCN $\nu_2 = 1-0$ fundamental and $\nu_2 = 2-1$ hot bands.

Figure 4.4 Examples of the fundamental $1-0$ band and the $2-1$ hot bands of the ν_5 C_2H_2 band (Figure 4.4(a)) and the ν_2 HCN band (Figure 4.4(b)). For both molecules the synthetic spectra are shown for temperatures of 10, 300 and 1000 K at a column density of $1.\,10^{16}\,\mathrm{cm}^{-2}$, $R = 1800$ and b=5 km s^{-1}. The shaded regions indicate the hot band absorptions (see Tables 4.2 and 4.3 for details). Note the difference in scale between Figure 4.4(a) and 4.4(b). In particular, note the $\nu_5 = 2-1$ C_2H_2 hot band at $13.89\,\mu$m. Although it is relatively weak compared to the fundamental $\nu_5 = 1-0$ C_2H_2 band its strength is of the same order as the ν_2 HCN bands.

A more detailed discussions on ro-vibrational lines and the use of band strengths, line strengths and partition functions can be found in Evans et al. (1991); Helmich (1996). They also list various conversions between units and notations used in the literature.

4.3.2 Hot bands

Some of the observed spectra (see §4.4) show evidence for gas at high temperatures up to 1000 K. At these temperatures the contribution of absorption from vibrationally excited states has to be considered, resulting in so-called "hot bands". To illustrate the effect of hot bands, Figure 4.4 shows the synthetic spectra of C_2H_2 and HCN at temperatures of 10, 300 and 1000 K. Table 4.3 lists the relative populations in the vibrationally excited levels and the strengths of the hot bands with respect to the fundamental $\nu_i = 1-0$ band at temperatures of 100, 300 and 1000 K for both HCN and C_2H_2. The $\nu_i = 2-1$ bands are of $\Sigma - \Pi$ and $\Delta - \Pi$ -type and are split in two close-lying transitions at $720\,\mathrm{cm}^{-1}$ ($13.89\,\mu$m) and $729\,\mathrm{cm}^{-1}$ ($13.72\,\mu$m) for C_2H_2 and $699.4\,\mathrm{cm}^{-1}$ ($14.30\,\mu$m) and $714.5\,\mathrm{cm}^{-1}$ ($14.00\,\mu$m) for HCN. It is seen that for HCN, the hot bands have nearly 75 % of the intensity of the fundamental band at $T \approx 1000$ K and significantly affect the spectra. For C_2H_2, the effect is smaller, but is still detectable at the $\sim 15\,\%$ level at the higher temperatures. Note that although the relative strength of the C_2H_2 hot band at $13.89\,\mu$m with respect to the fundamental band is small, its relative strength with respect to the HCN bands is larger since the C_2H_2 band is a factor of ~ 5 stronger than the HCN band. It is therefore important to include the C_2H_2 hot bands in the construction of the complete synthetic spectra.

Table 4.3. C_2H_2 and HCN $\nu_i = 1$ population and hot band strength

C_2H_2 $\nu_5 = 1$				HCN $\nu_2 = 1$			
	T_{ex} (K)				T_{ex} (K)		
	100	300	1000		100	300	1000
population[a]	.00006	.051	.09	population[a]	.00007	.062	.28
S^b ($720\,cm^{-1}$)	.00005	.042	.08	S^b ($699.4\,cm^{-1}$)	.00008	.035	.28
S^b ($729\,cm^{-1}$)	.00004	.023	.05	S^b ($714.5\,cm^{-1}$)	.00011	.071	.55

[a]Fractional population of $\nu_i = 1$ level

[b]Relative intensity with respect to fundamental band

The contribution of higher vibrational levels is small and the strength of the $\nu_i = 3 - 2$ bands is too small to be detected in these data. Thus, in the construction of the synthetic spectra no levels higher than the $\nu_i = 2 - 1$ bands are included. However, in calculating the population of the ground vibrational level, the populations of the higher levels are taken into account, since the population of the third vibrationally exited level can amount to 10 % for HCN.

4.3.3 Model fits

The parameters that enter the model fits are the excitation temperature(s) in K, the total column density in each temperature component in cm^{-2}, and the Doppler broadening parameter b of each component in km s^{-1}. The latter values can be constrained from high spectral resolution submillimeter lines of these sources, which indicate typical FWHM line widths $\Delta V = 1.665\,b$ of $3 - 4\,km\,s^{-1}$ for molecules such as $C^{17}O$ and HCN (van der Tak et al., 1999, 2000). Comparison with high resolution infrared spectra indicates that the latter lines are generally broader than the submillimeter lines. Thus, $b = 1.5\,km\,s^{-1}$ is taken as a lower limit in the model spectra, but values up to $b = 10\,km\,s^{-1}$ have been explored. The resulting Q-branch spectra show no significant variation over this range of b-values. Most of the presented spectra use $b = 5\,km\,s^{-1}$. At this value of b the C_2H_2 and HCN features stay optically thin at the inferred column densities and temperatures (see §4.3).

Fits of the model spectra to the observational data are made within the IDL package using the Powell optimisation routine. Different fits to the surrounding continuum were explored because of the uncertainty in the RSRF global shape. In some cases this improved the fits, but it had no major impact on the derived parameters. For each spectrum, fits were made with both a single temperature and with two temperature components. In the latter case, the two temperatures were taken from the Mitchell et al. (1990) study of CO and the column densities in each of the components were adjusted to give the best match to the spectrum. For the column densities involved, the absorptions of the two components are not saturated and can be added together in optical depth before convolution with the ISO-SWS Gaussian resolution.

Figure 4.5 shows the χ^2 distribution for one of the best sources, AFGL 2136. Illustrated here is a fit in HCN temperature and column density keeping the temperature and column density of C_2H_2 fixed at predefined values. Note that there is a clear

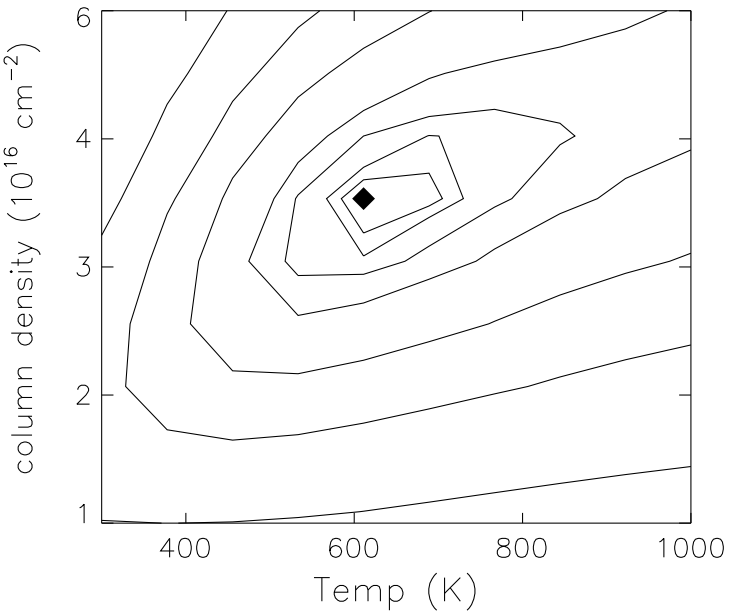

Figure 4.5 Example of χ^2 distribution in the case of AFGL 2136. Plotted are the minimum χ^2 (solid symbol) and the contours at 1.5, 2.5, 5, 10, 25, 50 and 100 % of the minimum χ^2. At the sampling of the spectrum used for this fit a χ^2 increase of 2.5 % corresponds roughly to a 3σ deviation of the model to the observed spectral feature.

correlation between the inferred temperature and column density. Asuming a higher temperature results in a higher

It should be emphasised that the ISO-SWS Q-branch spectra are of sufficiently high quality to allow the detection of even small amounts of C_2H_2 and HCN with column densities of a few $\times 10^{14}\,\mathrm{cm}^{-2}$ in very cold gas with $T = 10 - 20\,\mathrm{K}$ and small b-values of less than $2\,\mathrm{km\,s}^{-1}$. This is in contrast with asymmetric rotors such as H_2O without a Q-branch, where the ISO-SWS ν_2 data at $6\,\mu$m are primarily sensitive to much higher column densities in the warmer and/or less quiescent gas (Helmich, 1996).

4.4 Results

Table 4.4 summarises the best fit results for all targets, whereas the final spectra are presented in Figure 4.6. The upper half of Table 4.4 lists the best single temperature fit in which the excitation temperature and the column density are free parameters. The lower half gives a two temperature fit, in which the excitation temperatures are fixed at those found for CO by Mitchell et al. (1990) and the column densities are varied. Two component models in which both the temperature and column density are free parameters have been run as well, and provide slight improvements to the fits in some cases. However, the significance of the fit parameters for the second component is low and is therefore not given. The accuracy of the results for the low temperature

Table 4.4. Model fit[a] C_2H_2 and HCN excitation temperatures T_{ex} and column densities N

Target	C_2H_2[b]		HCN[b]	
	T_{ex} (K)	N 10^{16} (cm^{-2})	T_{ex} (K)	N 10^{16} (cm^{-2})
AFGL 2136	$800\pm^{150}_{100}$	1.5 ± 0.3	$600\pm^{75}_{50}$	3.5 ± 0.6
AFGL 2591	$900\pm^{150}_{120}$	2 ± 0.3	$600\pm^{75}_{50}$	4 ± 0.6
AFGL 4176 #1	$700\pm^{170}_{100}$	1 ± 0.2	$500\pm^{40}_{30}$	2 ± 0.4
AFGL 4176 #2	$700\pm^{250}_{150}$	1 ± 0.2	$500\pm^{50}_{50}$	2 ± 0.4
NGC 3576	$500\pm^{100}_{60}$	0.4 ± 0.1	$400\pm^{50}_{40}$	0.8 ± 0.3
NGC 7538 IRS 1	$800\pm^{250}_{150}$	0.8 ± 0.2	$600\pm^{50}_{40}$	1 ± 0.2
NGC 7538 IRS 9	$300\pm^{100}_{75}$	0.2 ± 0.1	$340\pm^{75}_{65}$	0.8 ± 0.3
W 33 A	$10\pm^{10}_{5}$	0.5 ± 0.2	$80\pm^{100}_{40}$	0.3 ± 0.2
W 3 IRS 5	$500\pm^{75}_{65}$	0.3 ± 0.1	$400\pm^{50}_{40}$	0.5 ± 0.1
S 140 IRS 1	–	–	–	–
G 333.3–0.4	300[e]	< 0.1	300[e]	< 0.3
AFGL 2059	10[e]	0.04 ± 0.04	10[e]	0.03 ± 0.03

	Fit using CO temperatures[c]					
	T^c_{cold} (K)	$N_{C_2H_2}$ 10^{16} (cm^{-2})	N_{HCN} 10^{16} (cm^{-2})	T^c_{hot} (K)	$N_{C_2H_2}$ 10^{16} (cm^{-2})	N_{HCN} 10^{16} (cm^{-2})
AFGL 2136	17	0.1	0.1	580	1.4	3.3
AFGL 2591	38	< 0.1	0.2	~ 1000	2.1	4.5
AFGL 4176 #1	–	–	–	≥ 500[d]	0.9	2.1
AFGL 4176 #2	–	–	–	≥ 500[d]	0.8	2.0
NGC 3576	–	–	–	≥ 500[d]	0.4	1.2
NGC 7538 IRS 1	25	< 0.05	< 0.05	176	0.3	0.4
NGC 7538 IRS 9	26	0.05	< 0.01	180	0.1	0.2
W 33 A	23	0.1	0.03	120	0.2	0.3
W 3 IRS 5	66	< 0.01	0.03	577	0.3	0.6
S 140 IRS 1	28	< 0.005	< 0.01	390	< 0.1	< 0.1
G 333.3–0.4	–	–	–	–	–	–
AFGL 2059	–	–	–	–	–	–

[a]For all fits, a Doppler parameter b=5 $km\,s^{-1}$ has been adopted

[b]Single component fits with both temperature and column density as free parameters

[c]Two component fits with temperatures fixed at the cold and hot temperatures found for CO by Mitchell et al. (1990)

[d]Temperature fixed at value indicated by the ISO–SWS CO spectrum

[e]Temperature fixed at assumed value

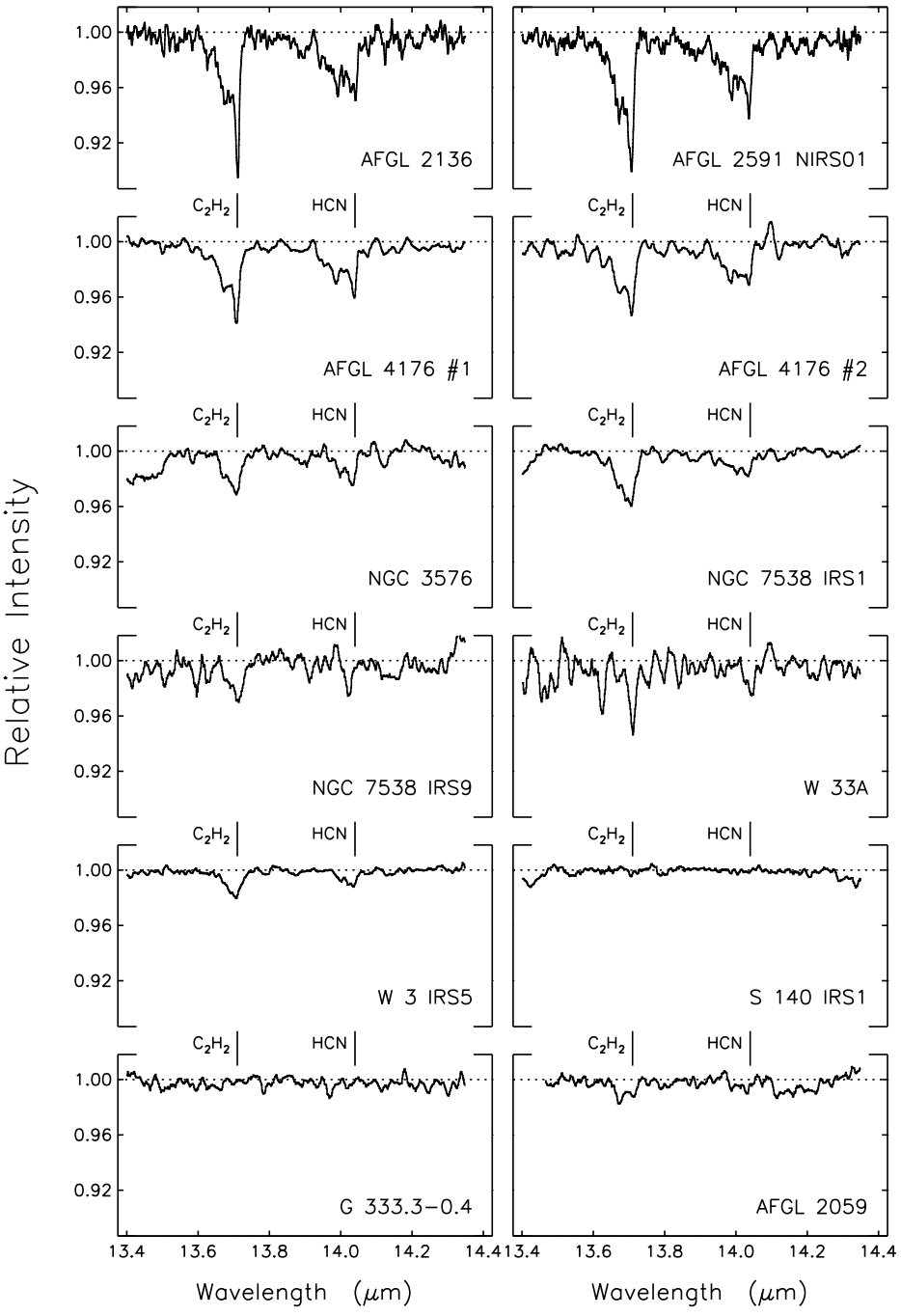

Figure 4.6 The final normalised spectra for all sources listed in Table 4.1. The positions of the ν_5 vibration-rotation band of C_2H_2 and the ν_2 vibration-rotation band of HCN are indicated.

component with $T_{\rm ex}$ fixed is also not high, but the results provide a good indication of the relative contributions from the cold and warm gas. Table 4.4 includes the 3σ error bars on the temperatures and column densities derived from the χ^2 fits for the single component fits and from comparison of different model fits.

For sources without a detection, the upper limits are based on an assumed temperature. Where available, this is taken to be the temperature of the warm CO given by Mitchell et al. (1990). In the case of G333.3-04, $T_{\rm ex} = 300\,{\rm K}$ is assumed. For AFGL 2059, the C_2H_2 spectrum hints at the presence of a cold gas component for which $T_{\rm ex}$ could be as low as a few K. The listed values assume $T_{\rm ex} = 10\,{\rm K}$ for both C_2H_2 and HCN to give an indication of the amount of cold gas, even though the uncertainty will be high.

No positive detection of $H^{13}CN$ at $14.165\,\mu$m has been made. A nominal ratio $H^{12}CN/H^{13}CN = 60$ would yield an absorption due to $H^{13}CN$ of only $0.5 - 1\,\%$. This is close to or below the limit at which a positive detection of an isolated spectral feature can be made at this wavelength. The absence of any $H^{13}CN$ absorption at the level of $\sim 2\,\%$ provides an independent confirmation that the Q-branch features are not highly optically thick.

In the following, the individual sources and spectra will be discussed in more detail, before turning to the more general discussion in §4.5.

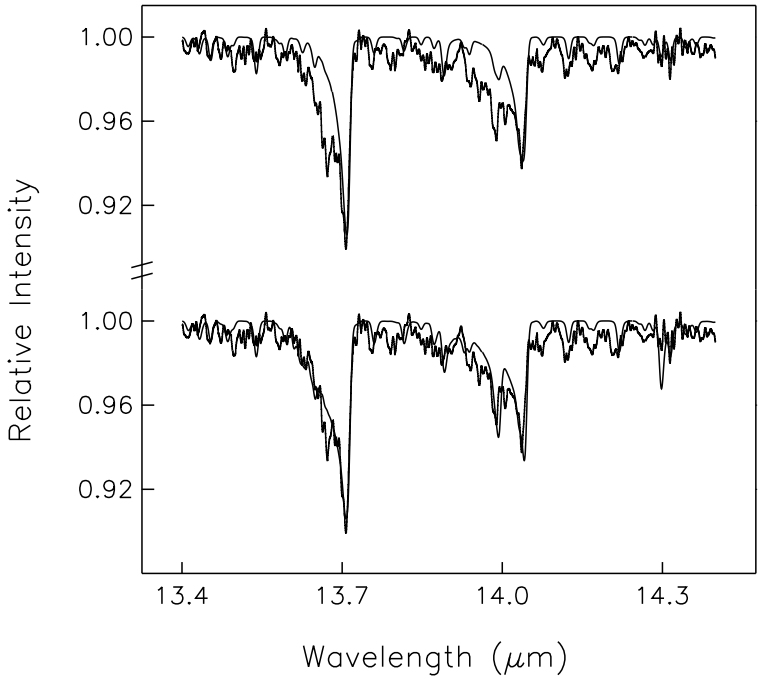

Figure 4.7 The upper plot illustrates a model fit for AFGL 2591 based on inferred temperatures and column densities by Carr et al. (1995). The lower plot illustrates a model fit based on temperatures and column densities inferred from the ISO-SWS spectrum (see Table 4.4).

4.4.1 AFGL 2591

The C_2H_2 and HCN Q-branches are clearly detected in the ISO-SWS data toward AFGL 2591. This is consistent with the ground-based results of Carr et al. (1995), who observed a number of low-J Q- and/or R-branch lines of C_2H_2 and HCN toward this object at higher spectral resolution. The inferred excitation temperatures and column densities are different, however. Carr et al. (1995) derived $T_{\rm ex} = 410\,{\rm K}$ and 340 K for C_2H_2 and HCN respectively, with column densities of $1.2\,10^{16}$ and $2.5\,10^{16}\,{\rm cm}^{-2}$. The top plot of Figure 4.7 shows the ISO-SWS spectrum compared to a model spectrum based on these temperatures and densities. It is clear that this model reproduces well the absorption of lines arising from lower J levels, but that an additional strong blue wing is seen in the ISO spectra for both molecules. The best-fitting single temperature results from the ISO data give 900 and 600 K, respectively, and the column densities are increased by a factor of two. The high temperatures are confirmed by the presence of hot bands in the spectra.

The ISO spectra of AFGL 2591 (see Figure 4.7 bottom plot), in particular the spectrum of C_2H_2, hint at the presence of a cold gas component ($10\,{\rm K} < T_{\rm cold} < 100\,{\rm K}$) in addition to the dominant hot ($\sim 1000\,{\rm K}$) component. At low temperatures the lower R-branch lines (for C_2H_2 at 13.625 and $13.67\,\mu$m) become more dominant (see Figure 4.4(a)). The temperature and column density of this cold gas are highly uncertain, however, because of the fringe residuals present in the spectrum. Nevertheless, the conclusion that the column density of the cold gas component for both C_2H_2 and HCN is only a small fraction ($\leq 10\,\%$) of that of the hot component is robust. A low temperature component with a significantly higher column density would have been readily detected (see the case of W 33 A).

4.4.2 AFGL 2136

The $13 - 15\,\mu$m ISO-SWS spectrum toward AFGL 2136 has been discussed previously by Boonman et al. (1999) in comparison with Orion IRc2/BN. Like AFGL 2591, this spectrum shows the presence of very warm C_2H_2 and HCN along the line of sight at temperatures of 800 and 700 K, respectively, with hot bands readily detected. The shape of the AFGL 2136 spectrum again hints at the presence of a small cold gas component with C_2H_2 and HCN column densities that are at most 10 % of those of the hot gas.

4.4.3 AFGL 4176

Two independent ISO-SWS spectra separated by almost one year have been taken toward the southern massive star-forming region AFGL 4176. The spectra agree well within the uncertainties of the calibration and data-reduction. Hot C_2H_2 and HCN are obviously present in both spectra, and the fit results agree within 10 % in derived temperature and column density. The only difference is the $\sim 50\%$ higher error on the temperature derived from the second observation.

4.4.4 W 33 A

W 33 A is one of the most luminous and massive objects in our sample, and lies in the direction of the Galactic center. Its infrared spectrum is characterised by very strong absorptions from interstellar ices seen from the ground (e.g. Willner et al., 1982; Allamandola et al., 1992) and by the ISO-SWS (e.g. Schutte et al., 1999; Gibb et al., 2000).

The $13-15\,\mu$m region of this object is interesting since it is the only case which shows a clear detection of cold C_2H_2 with $T_{\rm ex} \approx 10\,$K and possibly cold HCN at $T_{\rm ex} \approx 80\,$K. The inferred value of $N(C_2H_2)$ is sensitive to the adopted b-value (cf. Figure 4.3), and is increased by a factor of 2 if b=1.5 km s^{-1} rather than b=5 km s^{-1} is adopted. There is no definite detection of a warm component although it cannot be excluded. Upper limits on the warm C_2H_2 and HCN are a factor of 10 less than the column densities of warm gas found toward AFGL 2136 and AFGL 2591.

4.4.5 W 3 IRS 5

W 3 IRS 5 is also among the most luminous objects with a strong mid-infrared continuum. Large column densities of hot and cold CO have been detected along the line of sight by Mitchell et al. (1990), but the amount of hot and cold C_2H_2 and HCN is surprisingly low, nearly a factor of 5 less than found toward AFGL 2136 and AFGL 2591. A detailed JCMT 345 GHz line survey has been performed for this object by Helmich & van Dishoeck (1997), which also reveals low molecular abundances in general, except for sulfur-containing species.

4.4.6 NGC 7538 IRS 1 and IRS 9

The bright infrared sources in the massive star-forming region NGC 7538 provide an opportunity to compare the results for two massive YSOs which originate from the same parent cloud. The line of sight toward NGC 7538 IRS 9 is very rich in ices (e.g. Willner et al., 1982; Whittet et al., 1996), whereas that toward NGC 7538 IRS 1 has a much larger fraction of warm gas (Mitchell et al., 1990). This difference is also reflected in the C_2H_2 and HCN results: the excitation temperatures of both species are about a factor of 2 lower toward IRS 9. Nevertheless, the column densities of warm C_2H_2 and HCN are comparable in the two sources. Cold HCN seems to have very low abundances in both cases.

4.4.7 Other sources

Of the remaining sources, only the southern object NGC 3576 shows a clear detection of hot C_2H_2 and HCN, in agreement with the detection of hot CO along this line of sight in the ISO spectra. The spectrum of AFGL 2059 shows absorption peaks at the wavelengths of C_2H_2 and HCN and bluewards, which may indicate the presence of a cold component. However the quality of the spectra is insufficient to determine reliable temperatures and column densities. Column densities are derived at an assumed temperature to give an indication of the amount of cold gas. The upper limits on the column densities toward S 140 and G333.3-0.4 are about an order of magnitude lower than the column densities found toward AFGL 2136 and AFGL 2591.

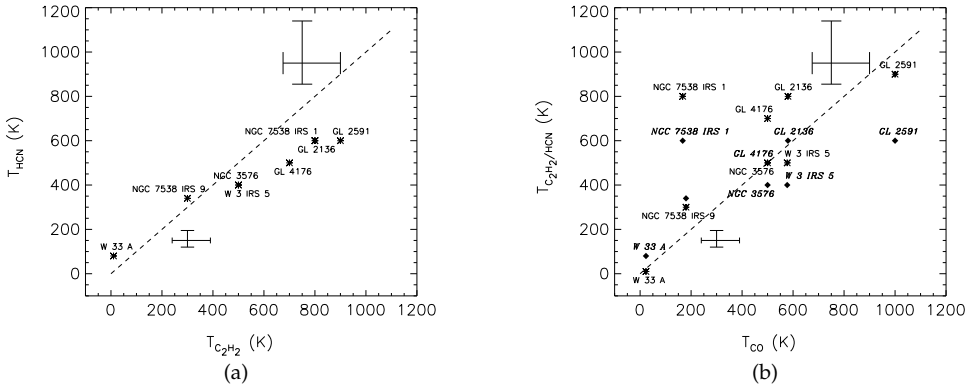

Figure 4.8 (a) Derived C_2H_2 excitation temperature versus derived HCN excitation temperature. (b) Inferred C_2H_2 and HCN excitation temperatures versus observed excitation temperature of the hot CO component (except for W 33A) by Mitchell et al. (1990). The C_2H_2 excitation temperatures are plotted as asterisks and the HCN excitation temperatures as diamonds.

4.5 Discussion

A few general conclusions are apparent from the above results (see Table 4.4). First, gas-phase C_2H_2 and HCN are detected for at least two-thirds of the sources. Second, where detected, the single temperature fits indicate high temperatures of $300 - 1000$ K. The only clear exception is formed by W 33 A. Third, the column densities of cold C_2H_2 and HCN in the two temperature fits are generally an order of magnitude lower than the column densities found in the hot component. The main exception is again W 33 A. Fourth, the column densities and abundances increase with increasing excitation temperature, but there is no correlation with luminosity of the object. In the following, the results on the excitation temperatures and column densities are discussed in more detail.

4.5.1 Excitation temperature

In Figures 4.8(a) and 4.8(b), the inferred C_2H_2 and HCN excitation temperatures are compared with each other and with the temperatures determined from the CO infrared observations of Mitchell et al. (1990). Except in the case of W 33 A, the temperature of the hot CO component is used in the comparison, since mostly hot C_2H_2 and HCN is observed. The derived C_2H_2 and HCN excitation temperatures correlate well with each other (a correlation coefficient of 0.98), whereas the correlation with the CO excitation temperatures is lower (correlation coefficients of 0.69 for C_2H_2 and 0.62 for HCN). C_2H_2 and HCN are probably cleaner tracers of the hot gas than CO, because their abundances are enhanced by two orders of magnitude compared with the cold gas (see §4.5.2). In contrast, the CO abundance is not expected to vary by more than a factor of two between the cold and hot components, as long as the temperature is high enough ($>$ 20 K) to prevent freeze-out of the molecule.

The differences in excitation temperature may also reflect different excitation mechanisms of the molecules. The two principal processes are collisional excitation in warm,

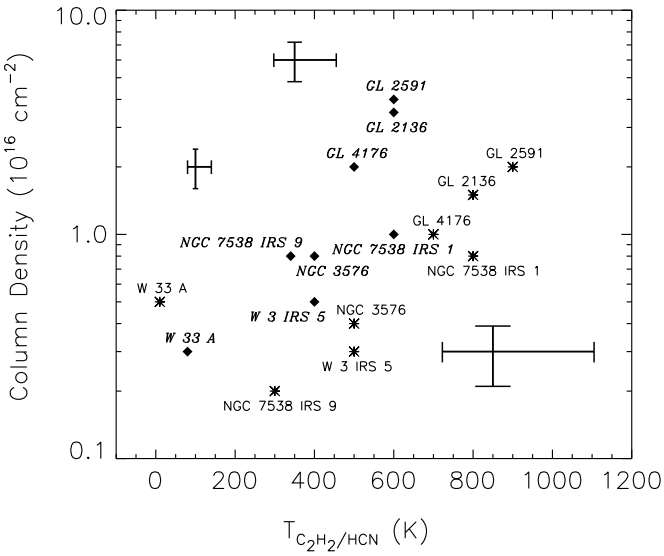

Figure 4.9 Column densities of C_2H_2 and HCN as functions of their excitation temperature. The column densities of C_2H_2 are shown as asterisks and the column densities of HCN as diamonds.

dense gas and radiative excitation by infrared radiation due to warm dust. In contrast with C_2H_2, HCN has a large dipole moment so that its rotational energy levels can relax rapidly through spontaneous emission. Thus, any non-LTE effects on the excitation are expected to be much larger for HCN. The fact that the HCN and C_2H_2 excitation temperatures are similar indicates that either the density is much above the critical density of the high-J levels or that the radiative excitation rates are much more rapid than relaxation rates, so that the excitation temperatures reflect the colour temperature of the radiation field rather than the kinetic temperature. Both HCN and C_2H_2 can be efficiently pumped through the ν_2 and ν_5 bands at $14\,\mu$m. In contrast, CO can only be pumped through its vibrational transition at much shorter wavelengths around $4.6\,\mu$m.

A rough estimate of the relative importance of the collisional and radiative rates can readily be made. Consider as an example a high-J level of HCN, say $J = 10$, which lies at 234 K above ground. In gas with temperatures > 100 K, collisional excitation occurs at a rate of $\sim 2 \times 10^{-10}\, n\,\mathrm{s}^{-1}$. The spontaneous emission rate to lower levels is $A(J = 10 \rightarrow 9) = 4.6 \times 10^{-2}\,\mathrm{s}^{-1}$. The mid-infrared continuum of the observed sources is due to emission from warm dust and can be fitted by blackbody emission with temperatures ranging from 50 K at long wavelengths to 700 K at the shorter wavelengths. At 300 K, the radiative excitation rate of HCN through the ν_2 vibrational band with $A_{1\rightarrow 0} = 3.2\,\mathrm{s}^{-1}$ is $\sim 10^{-1}\,\eta\,\mathrm{s}^{-1}$, where η is a geometrical dilution factor. The HCN rotational excitation can therefore either be produced by collisions in warm gas with densities of order $10^9\,\mathrm{cm}^{-3}$ or by radiative excitation in lower density gas. In the power-law density model of AFGL 2591 by van der Tak et al. (1999), the density reaches 10^9 cm^{-3} only at unrealistically small distances of <10 AU, so that radiative pumping likely dominates. For C_2H_2, the infrared pumping rate is comparable. For CO, however, the radiative

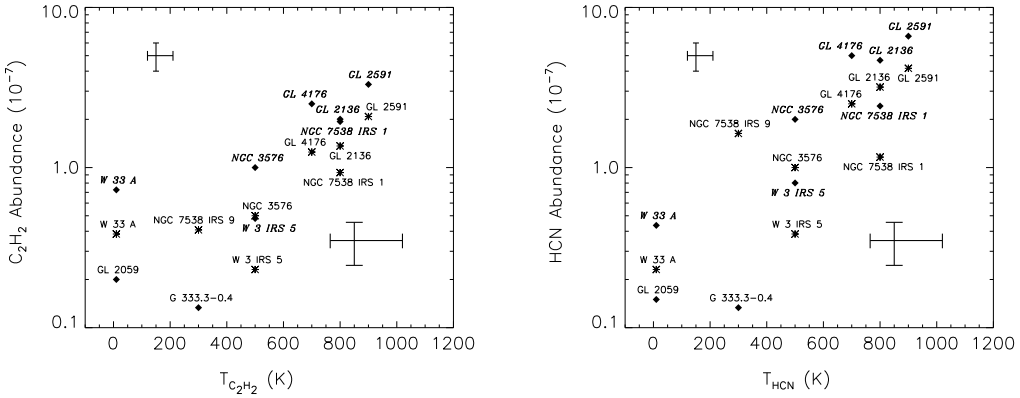

(a) C_2H_2 abundance (b) HCN abundance

Figure 4.10 The C_2H_2 and HCN abundances as functions of excitation temperature. The abundances are shown with respect to the hot H_2 component (diamonds) and the total H_2 (asterisks).

excitation rate at $4.6\,\mu$m is at least two orders of magnitude lower, so that collisional excitation dominates over a larger fraction of the envelope for this molecule, leading to more direct constraints on kinetic temperature and density.

The low HCN and C_2H_2 excitation temperatures for W 33 A compared with other sources of similarly high luminosity are puzzling. The CO data indicate warm gas toward this source, but with temperatures only up to $\sim 120\,$K. The detection of high excitation lines of CH_3OH at submillimeter wavelengths indicates that warm gas with $T_{\rm ex} \approx 150\,$K is present in the inner region (van der Tak et al., 2000). Either the source has only just started to evaporate the ices, or the more massive envelope results in a high optical depth at mid-infrared wavelengths, preventing observations of the inner, warmer gas.

4.5.2 Column densities and abundances

In Figure 4.9, the inferred column densities of C_2H_2 and HCN are shown as functions of the derived excitation temperatures of the molecules. Both species show a clear increase by nearly two orders of magnitude in the warmer gas. The corresponding abundances in the warm gas have been determined using the column densities of warm H_2 derived from the ^{13}CO column densities of Mitchell et al. (1990) assuming an abundance ratio $^{13}{\rm CO}/{\rm H_2} = 3.3 \times 10^{-6}$. For sources not observed by Mitchell et al. (1990), the total H_2 column density has been constrained from the $C^{17}O\,2-1$ emission line observed with the 15m SEST telescope and/or from the silicate optical depth observed by Willner et al. (1982). Since these sources are among the hottest sources, it is assumed that at least 50 % of the gas is in the "warm" component.

Table 4.5 list the total H_2 column densities, the fraction of hot H_2, and the corresponding C_2H_2 and HCN abundances. Figures 4.10(a) and 4.10(b) include the abundances of the molecules as functions of excitation temperature. The C_2H_2 and HCN abundances increase from 10^{-8} to 10^{-6}, with HCN a factor of a few more abundant

Table 4.5. C_2H_2 and HCN abundances with respect to total H_2 and hot H_2.

Target	$H_{2\,\mathrm{tot.}}$ [a]	x_{hot} [b]	C_2H_2 abundance (10^{-7})		HCN abundance (10^{-7})	
			total H_2	hot H_2	total H_2	hot H_2
AFGL 2136	11.	0.68	1.4±0.3	2.0±0.2	3.2±0.6	4.7±0.8
AFGL 2591	9.6	0.63	2.1±0.3	3.3±0.5	4.2±0.6	6.6±1.0
AFGL 4176 #1	8.0	0.5[e]	1.3±0.3	2.5±0.5	2.5±0.5	5.0±1.0
AFGL 4176 #2	8.0	0.5[e]	1.3±0.3	2.5±0.5	2.5±0.5	5.0±1.0
NGC 3576	8[c]	0.5[e]	0.5±0.1	1.1±0.3	1.0±0.4	2.0±0.8
NGC 7538 IRS 1	8.6	0.48	0.9±0.2	1.9±0.5	1.2±0.2	2.4±0.5
NGC 7538 IRS 9	4.9	0.02	0.4±0.2	20±10	1.6±0.6	80±30
W 33 A	13.	0.53	0.5±0.2	1.0±0.4	0.2±0.1	0.4±0.3
W 3 IRS 5	13.	0.48	0.3±0.1	0.5±0.2	0.5±0.1	0.8±0.2
S 140 IRS 1	3.7	0.60	< 0.5	< 1.0	< 2.0	< 3.0
G333.3–0.4	15[c]	0.5[e]	< 0.1	< 0.2	< 0.2	< 0.4
AFGL 2059	4[d]	0.5[e]	0.1±0.1	0.2±0.2	0.1±0.1	0.2±0.2

[a]Total H_2 column density in $10^{22}\,\mathrm{cm}^{-2}$ derived from ^{13}CO observations by Mitchell et al. (1990), assuming $^{12}\mathrm{CO}/^{13}\mathrm{CO} = 60$ and $^{12}\mathrm{CO}/\mathrm{H}_2 = 2.\,10^{-4}$.

[b]Fraction of hot H_2, $x_{hot} = N_{hot}(H_2)/N_{tot}(H_2)$

[c]From SEST $C^{17}O$ 2–1 data

[d]Based on 9.7 optical depth (Willner et al., 1982)

[e]Estimate

than C_2H_2. At the highest temperatures, these molecules are among the most abundant carbon- and nitrogen-bearing molecules. The largest deviations are provided by NGC 7538 IRS1 and W 3 IRS5, where the HCN and C_2H_2 abundances are remarkably low for the high inferred excitation temperatures. For NGC 7538 IRS1, the HCN and C_2H_2 abundances would be consistent with the relation found for other sources if the lower excitation temperature of 180 K derived from CO is adopted. The data for G 333.3-0.4 are upper limits with an assumed temperature of 300 K.

The column densities and abundances of C_2H_2 and HCN in the cold gas component are only poorly constrained by our low-resolution data, but are at least an order of magnitude lower than those in the hot component. From detailed modeling of the submillimeter line emission, van der Tak et al. (1999, 2000) derive typical HCN abundances of a few $\times 10^{-9}$ in the extended envelope, similar to the values found here. The inner, warm region around AFGL 2591 has been probed with the OVRO millimeter array in the HCN $1-0$ emission line. The fact that these interferometer data do not show enhanced HCN abundances indicates that the source size of the abundant HCN seen by ISO is restricted to less than 300 AU (van der Tak et al., 1999).

4.5.3 Chemistry

Steady-state gas-phase chemistry models of cold, dense clouds give typical HCN abundances of a few $\times 10^{-9}$ and C_2H_2 abundances ranging from $10^{-9} - 10^{-8}$, depending on the importance of destruction by neutral-neutral reactions with atomic C (Lee et al., 1996; Millar et al., 1997). These model results are consistent with our observed abundances in the cold gas.

Increasing the temperature in these pure gas-phase models to $\sim 200\,\mathrm{K}$ does not significantly affect the abundances of the molecules in steady-state. Higher abundances are found in time-dependent models at early times, if the gas is initially atomic carbon rich. However, neither C_2H_2 nor HCN reach abundances as high as a few $\times 10^{-7}$ in these models. Also, the limits on the observed atomic carbon column density for these sources rule out these models (van der Tak, private communication).

More relevant for the chemistry in the warm gas are the so-called 'hot core' models, in which ice mantles are sublimated from the grains into the gas (e.g. Millar et al., 1991; Charnley et al., 1992; Helmich, 1996; Charnley, 1997). The evaporated molecules subsequently drive a rapid gas-phase chemistry in the dense, warm gas resulting in complex organic molecules for a period of $\sim 10^5\,\mathrm{yr}$. None of these hot core models shows efficient C_2H_2 production in the warm gas, however. Thus, in order to explain the observed high C_2H_2 abundances of 10^{-7}, the molecule must originally be present in the ices on the grains. Solid C_2H_2 has not yet been detected, but the observed limits are not very stringent, since C_2H_2 mixed in H_2O ice does not have strong spectral signatures (Boudin et al., 1998, Schutte 1998, private communication,). The inferred ratio for the ices, $C_2H_2/H_2O < 0.1$, corresponds to $x(C_2H_2) < 10^{-5}$. Our observed C_2H_2 abundances of $\sim 10^{-7}$ are $1-2$ orders of magnitude lower. They can be explained if the molecule is present at an abundance of $0.1 - 0.5\,\%$ relative to H_2O in the ices and if the time scale since evaporation is less than 10^5 yr. C_2H_2 has been observed in cometary ices with an abundance of $0.1 - 0.9\,\%$ with respect to H_2O (Brooke et al., 1996; Bockelée-Morvan et al., 2000), providing support for this picture.

Solid HCN has also not been detected in interstellar ices, at abundances down to $\sim 3\,\%$ of H_2O ice (Schutte 1998, priv. comm., using data from Bernstein et al., 1995). The corresponding abundance with respect to H_2 of a few $times 10^{-6}$ is somewhat higher than the highest observed gas-phase HCN abundances in this work. If the molecule were present at the level of $\sim 0.5\,\%$ in the ices, evaporation could explain our observed abundances. The observed HCN abundance in comets is slightly lower, $0.05 - 0.25\,\%$ (Irvine & Bergin, 2000; Bockelée-Morvan et al., 2000). In contrast with C_2H_2, HCN does participate actively in the high-temperature gas-phase chemistry. Indeed, van der Tak et al. (1999) argue from their HCN interferometer results that the high gas-phase HCN abundances observed by ISO cannot just be the result of grain mantle evaporation but that gas-phase chemistry must play a role as well. At high temperatures $> 300\,\mathrm{K}$, a large fraction of the oxygen is thought to be driven into gas-phase H_2O through the $O + H_2$ and $OH + H_2$ reactions. This results in a low gas-phase O_2 abundance, one of the principal destroyers of atomic C. The gas-phase HCN abundance is significantly increased with enhanced atomic C and N abundances. An alternative mechanism to enhance HCN would be through evaporation of NH_3 from the ices, followed by subsequent gas-phase reactions leading to HCN, similar to the case of the Orion hot core (Charnley et al., 1992). More detailed modeling of the HCN chemistry in hot cores up to temperature of 1000 K is needed to further interpret the results.

The sources with the highest HCN and C_2H_2 abundances are also those with the highest gas-phase H_2O abundances (e.g. van Dishoeck, 1998) and those which show the largest fraction of heated ice (Boogert et al., 2000; Gerakines et al., 1999). Since these diverse phenomena involve a range of temperatures from $< 100\,\mathrm{K}$ to 1000 K, this indicates that the enhanced temperatures are communicated to both the inner and the outer parts of the envelope. van der Tak et al. (2000) suggest that this 'global heating' results from the gradual dispersion of the envelope with time, resulting in a lower ratio of envelope mass to stellar mass and higher temperatures throughout the envelope.

4.6 Conclusions

The main conclusions of our work can be summarised as follows:

- Gas-phase C_2H_2 and HCN have been detected toward two-thirds of the high-mass YSOs studied in this work.
- Where detected, the excitation temperatures of C_2H_2 and HCN are high, up to 1000 K. The only exception is formed by W 33A. The temperatures derived from the C_2H_2 and HCN data correlate well with each other (with a correlation coefficient of 0.98). The correspondence with the CO excitation temperature is slightly worse, indicating that these two molecules may be better probes of the hot core gas in massive YSOs.
- Except for W 33A, the C_2H_2 and HCN column densities in the cold ($< 80\,\mathrm{K}$) gas are at least an order of magnitude lower than those in the hot gas.
- The C_2H_2 and HCN abundances in the hot gas show a clear increase with excitation temperature from 10^{-8} to 10^{-6}. For C_2H_2, such high abundances are plausibly explained by a passive hot core model, in which C_2H_2 is directly evaporated from the ices. The required C_2H_2 ice abundance of $0.1 - 0.5\,\%$ with respect to H_2O ice is consistent with that found for cometary ices. For HCN, a combination of ice evaporation and high temperature gas-phase reactions likely plays a role.

The gas-phase HCN and C_2H_2 data presented here strengthen the picture based on other ISO observations that the heating of the surrounding envelope by the YSO and evaporation of ices play a dominant role in the physical and chemical evolution of these massive YSOs.

Acknowledgements

The data presented here were analysed with the support of the Dutch ISO Data Analysis Centre (DIDAC) at the Space Research Organisation Netherlands (SRON) in Groningen, the Netherlands. The authors are grateful to Frank Helmich, Annemieke Boonman and John Black for their help with the construction of the model spectra, to Willem Schutte for limits on the ices, to Floris van der Tak, Adwin Boogert, Pascale Ehrenfreund, Thijs de Graauw, Jacquie Keane, Do Kester, Xander Tielens, Doug Whittet and the members of the ex-SIDT in VILSPA for many useful discussions, and to Michiel Hogerheijde for obtaining the SEST spectra. This work was partly supported by NWO grant 614.41.003.